ADVANCED HEALTHCARE MATERIALS
www.advhealthmat.de

Nature-Skin-Derived e-Skin as Versatile "Wound Therapy-Health Monitoring" Bioelectronic Skin-Scaffolds: Skin to Bio-e-Skin

Xinhua Liu, Boqiang Cui, Xuechuan Wang, Manhui Zheng, Zhongxue Bai, Ouyang Yue, Yifan Fei, and Huie Jiang**

Electronic skins (e-skins) have the potential to turn into breakthroughs in biomedical applications. Herein, a novel acellular dermal matrix (ADM)-based bioelectronic skin (e-ADM) is used to fabricate versatile "wound therapy-health monitoring" tissue-nanoengineered skin scaffolds via a facile "one-pot" bio-compositing strategy to incorporate the conductive carbon nanotubes and self-assembled micro-copper oxide microspheres with a cicada-wing-like rough surface and nanocone microstructure. The e-ADM exhibits robust tensile strength (22 MPa), flexibility, biodegradability, electroactivity, and antibacterial properties. Interestingly, e-ADM exhibits the pH-responsive ability for intelligent command between sterilization and wound repair . Additionally, e-ADM enables accurate real-time monitoring of human activities, providing a novel flexible e-skin sensor to record injury and motions. In vitro and in vivo experiments show that with electrical stimulation, e-ADM could prominently facilitate cell growth and proliferation and further promote full-thickness skin wound healing, providing a comprehensive therapeutic strategy for smart sensing and tissue repair, guiding the development of high-performance "wound therapy-health monitoring" bioelectronic skin-scaffolds.

1. Introduction

Wearable bioelectronics enables monitoring of the intermolecular electron transfer in physiological processes and provides real-time physical and (bio)chemical sensing, providing the foothold for developing bioelectronics for biomedical applications.[1,2] The skin is widely acknowledged as the largest human organ, and its natural multi-hierarchical barrier to the external environment is often deemed the ideal human–machine interface.[3,4] Research in skin-integrated electronics (called "electronic skin") has the potential to revolutionize biomedical applications, including wearable health monitoring, regenerative biomaterials, and diagnostics, given their capacity to bio-simulate and elevate the external perception of human skin.[5,6]

From the perspective of real-world biomedical applications, it is paramount that electronic skin (e-skin) should not only possess reliable mechanical properties, including favorable stretchability and high mechanical strength but integrate intelligent sensing ability and various biological functions, especially for antibacterial activity and tissue repair for comprehensive therapy of skin wounds with full-thickness or extensive defects.[7,8] The leap from e-skin to bio-e-skin is that bio-e-skin skin can be widely used to accelerate tissue healing and functional recovery. Compared with normal sensing devices (e-skin), bio-e-skin has better biocompatibility and can accelerate wound healing by promoting cell proliferation, secreting growth factors, synthesizing extracellular matrix (ECM), and revascularization. Compared with wound repair materials,[9] bio-e-skin can monitor the subtle movement of the wound and show the potential to benefit the wound treatment process. The input of biomimetic microcurrent can effectively accelerate the repair of severe tissue damage.[10] Our previous work provides a new way to explore more nature-inspired multifunctional bioelectronic skin for biomedical applications.[11,12] However, e-skin exhibits a limited ability to meet the complex requirements of wound repair, such as biocompatibility, antibacterial properties, mechanical properties, and other manipulations of the microenvironment, that affect the wound healing process.[13] Significant inroads have been achieved in recent years with the design of e-skin integrating the topology, mechanical cues, chemical, and electrical properties for monitoring complex physiological activities and intervening in regulatory cell activities for the specific biological application requirements under bioelectrical stimulation (ES).[14] It is well-established that bioelectricity maintains the excitability of various cells, regulates the cell proliferation cycle, and occurs in every somatic cell. Accordingly,

X. Liu, B. Cui, X. Wang, M. Zheng, Z. Bai, Y. Fei, H. Jiang
College of Bioresources Chemical and Materials Engineering
Institute of Biomass & Functional Materials
Shaanxi University of Science & Technology
Xi'an 710021, P. R. China
E-mail: liuxinhua@sust.edu.cn; jianghuie@sust.edu.cn
X. Liu, X. Wang, O. Yue
College of Chemistry and Chemical Engineering
Shaanxi University of Science & Technology
Xi'an, Shaanxi 710021, P. R. China

The ORCID identification number(s) for the author(s) of this article can be found under https://doi.org/10.1002/adhm.202202971

DOI: 10.1002/adhm.202202971

imparting exogenous ES to the wound tissues urges cells into an excited state and accelerates cell growth and proliferation to further promote wound healing and tissue regeneration.[15] With the integration of the ES for wound healing, next-generation tissue-engineered skin scaffolds promise to achieve comprehensive therapeutic effects under electrical stimulation integrated with curative functionalities such as intelligent sensing, affluent biological functions, and antibacterial and mechanically flexible properties.[16,17]

Screening and manufacturing new intelligent flexible biocompatible substrate materials is the key to constructing e-skin matching real-world biomedical applications. Over the years, flexible substrate materials have been used for manufacturing e-skin including polydimethylsiloxane,[18] polyurethane,[19] rubber, polyester,[20] polyamide, and cellulose.[21] In general, the biocompatibility, biodegradability, hygienic performances, and wearing comfort of polymer-based e-skin have vastly limited their biomedical applications. In recent years, acellular dermal matrix (ADM), a derivative of natural skin, has been regarded as an alternative to "gold standard" tissue grafts given its excellent physicochemical and biological properties, which have been harnessed in wound repair, homeostasis maintenance, the filling of tissue defects, cell delivery via scaffold, etc.[22] Specifically, ADM is prepared from animal skins through a series of physical, chemical, and biological methods to remove disparate somatic cells and other immunogens from the skin dermis, and thus mainly remains the natural collagen micro-nano fiber scaffolds with the complex 3D structure of the skin.[23,24] Importantly, the Glycine-Histidine-Lysine (GHK) tripeptide produced by ADM degradation can promote the synthesis of collagen,[25] mucopolysaccharide, and proteoglycan, and ADM maintains its biological activity by adhering to platelet-derived growth factor (PDGF). These observations highlight the need to develop a novel ADM-based e-skin that can harvest the inherent advantageous properties of natural building blocks with high mechanical flexibility, electrical conductivity, biocompatibility, biodegradability, hygiene, and wearing comfort.[7,26,27]

Copper has been used as a broad-spectrum and efficient fungicide for more than 200 years. Indeed, the antibacterial ability of copper is not inferior to silver and zinc ions. Furthermore, overwhelming evidence substantiates that low concentrations of copper ions can stimulate endothelial cell proliferation and migration,[28,29] promote the formation of new blood vessels, and inhibit vascular smooth muscle cell proliferation and thrombosis. Based on copper's biological functions and benefits, much emphasis has been placed on developing new copper-containing biomaterials.[30,31]

It is well-recognized that the relatively rough surface and the nanocone with a height of about 200 nm of cicada wings endow them with antibacterial ability by producing shear force to destroy the bacteria's cell wall.[32,33] Copper oxide microspheres have a more stable structure than other shapes such as nanorods.[34] The appropriate size can ensure that they are interspersed between fiber bundles. The protrusions on the surface of the microspheres will bring a better copper ion release effect[35] and kill bacteria by physical means.[36] Herein, by integrating the inherent advantageous high-performances of natural ADM and the antibacterial activity of cicada wing, a novel ADM-based bioelectronic skin (e-ADM, also referred to as bio-e-skin) was fabricated to obtain versatile "wound therapy-health monitoring" tissue-nanoengineered skin-scaffolds. The "one-pot" bio-compositing strategy of nature ADM was used to incorporate the functional building blocks of conductive carbon nanotubes (CNTs) and self-assembled micro-copper oxide microspheres with a cicada-wing-like rough surface and nanocone microstructure. The interactions among the CNTs, micro-copper oxide microspheres, and collagen nanofibers of ADM in e-ADM provide an integrative crosslinking strategy to establish a fibrous 3D network with structural and functional stability. With this multifunctional and bionic-structure design, our e-ADM exhibited robust tensile strength (22 MPa), antibacterial properties, and the pH-responsive ability for intelligent command between sterilization (pH ≈5–6) and wound repair (pH 7.4). In addition, e-ADM can monitor large-scale human motion in real-time. Compared with traditional sensing devices, it has the general compatibility and toughness of natural skin, can ensure the stability of sensing devices, can better fit with the skin, and can more accurately identify some subtle movements (such as throat and chewing), showing the potential of new flexible electronic skin to record injuries and movements.[37] Additionally, e-ADM equipped with precise electrical stimulation can promote cell growth and proliferation and promote full-thickness skin wound healing, leading to novel versatile and flexible "wound therapy-health monitoring" bioelectronic skin (bio-e-skin) with on-demand high-performance for real-world biomedical applications.

2. Results

2.1. Design and Fabrication of μCuO Microspheres and e-ADM

The proposed e-ADM was fabricated through a facile "one-pot" bio-compositing strategy by incorporating the functional building blocks (conductive CNTs) and self-assembled micro-copper oxide microspheres with a cicada-wing-like rough surface and nanocone microstructure. The copper microspheres prepared by the hydrothermal method exhibited a cicada-wing-like structure (**Figure 1**A) and uniform particle size distribution.[38,39] During the hydrothermal reaction, a copper oxide cone column of about 200 nm (Figure 1B) is formed and self-assembled into microspheres of about 5 μm diameters (Figure 1C), so that the antibacterial mechanism can be exerted both physically (Figure 1D) and chemically (Figure 1E), allowing the effective release of ions. After the introduction of CNTs, the conductivity and antibacterial ability of ADM scaffolds were further improved. The two materials in ADM were mainly physically bound by hydrogen bonding, electrostatic adsorption, physical permeation, and diffusion. CNTs were closely attached to the micro-nano fibers of ADM to form a continuous conductive layer due to their small size. Copper microspheres were combined between micro-nano fibers in the form of intercalation and adsorption (Figures 1F and **2**A). A 3D amorphous fiber network weaving structure was formed with a certain amount of micropores (**Figure 2**B,C), which is conducive to the proliferation and growth of cells. The above structures of skin scaffolds were further fixed after freeze-drying (Figure 2D). A series of physical images of skin scaffolds are shown in Figure S2, Supporting Information.

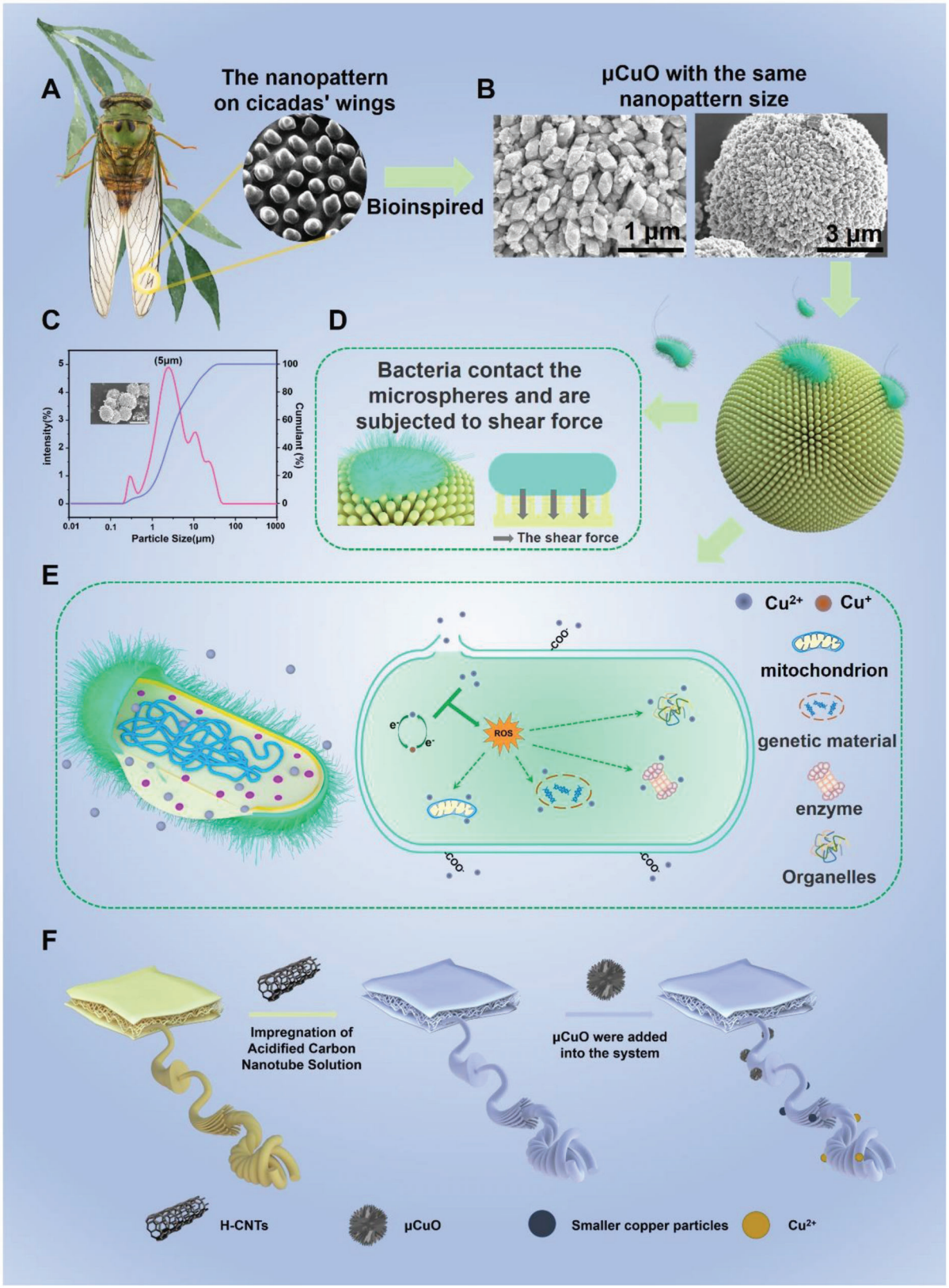

Figure 1. Design inspiration, preparation scheme, and antibacterial mechanism of μCuO microspheres. A) Unique nanocolumnar structure of cicada wing. B) Surface morphology of μCuO microspheres. C) Particle size test results of μCuO microspheres. D) Physical antibacterial mechanism of μCuO microspheres. E) Chemical antibacterial mechanism of μCuO microspheres. F) Design strategy of e-ADM.

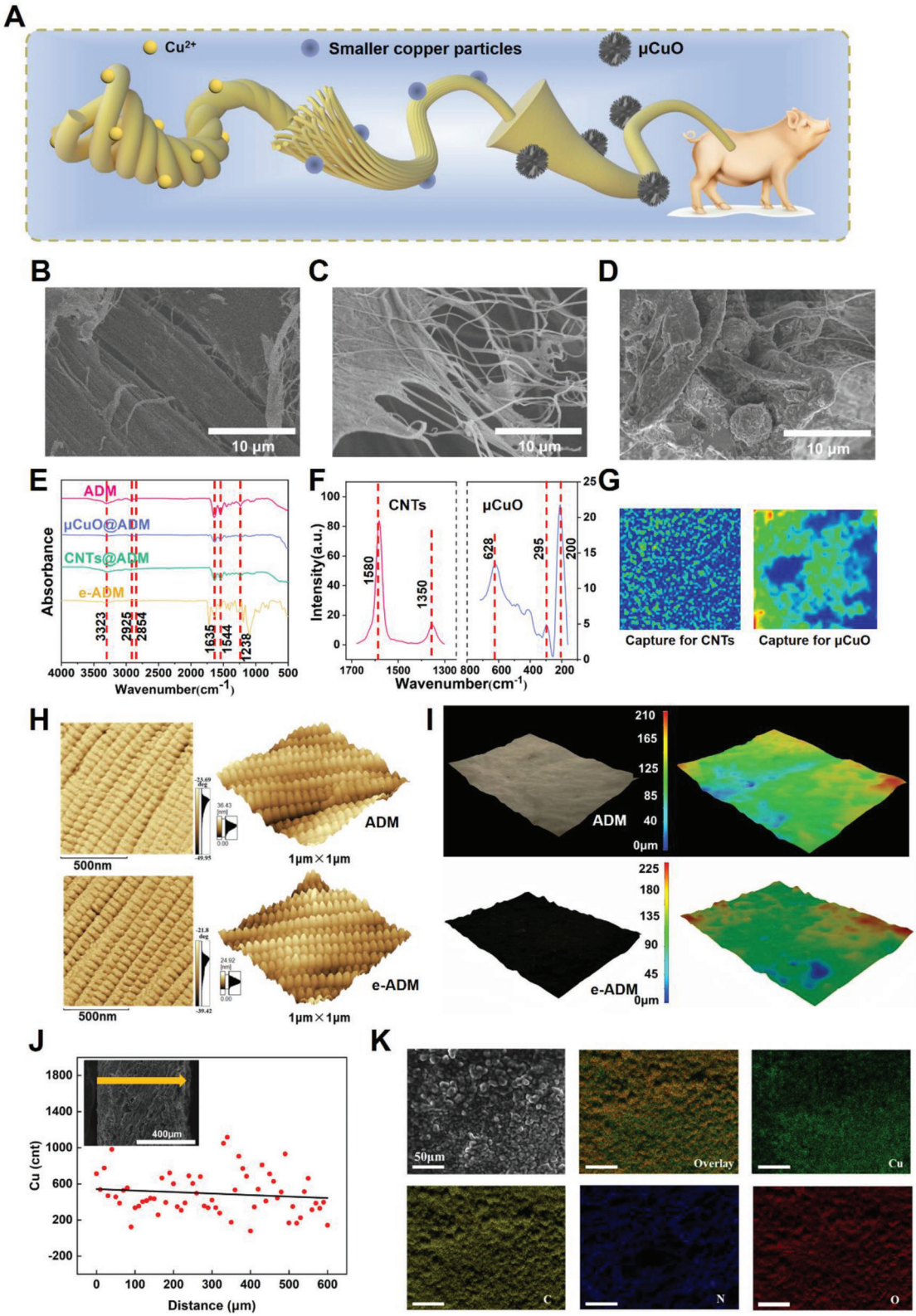

Figure 2. Structural characterization of e-ADM. A) Multi-level structure of ADM. B) Structural photos of ADM internal collagen fibers tightly woven. C) SEM images of collagen fiber bundles in ADM. D) Internal structure photos of e-ADM after freeze-drying. E) Infrared spectra of a series of skin scaffolds. F) Raman spectra of e-ADM. G) Raman mapping images of e-ADM. H) AFM observation images of ADM and e-ADM. I) Super depth of field observation images of ADM and e-ADM. J) Cross-sectional spectral line scan images and element distribution results of e-ADM. K) Surface spectral surface scan results of e-ADM.

Fourier transform infrared spectroscopy (FT-IR) was used to reflect the secondary structure of proteins (Figure 2E). ADM collagen protein was composed of more than 20 kinds of α-amino acids. The main groups and structures of α-amino acids are methylene, carboxyl, and amino groups. The stretching vibration characteristic peak of $-NH_2$ was observed near 3323 cm^{-1}, and the asymmetric stretching vibration and symmetric stretching vibration characteristic absorption peaks of $-CH_2-$ appeared at 2925 and 2854 cm^{-1}, respectively. The shear vibration characteristic absorption peak appeared near 1452 cm^{-1}. The characteristic absorption peak of carbonyl stretching vibration in the carboxyl group was around 1635 cm^{-1}, forming the strongest absorption band (the amide I band). The characteristic absorption peaks of –CN– stretching vibration and –NH– shearing vibration appeared at 1544 cm^{-1}, forming a strong absorption band (the amide II band); the characteristic absorption peaks of carbonyl stretching vibration and carbon and amine stretching vibration in carboxyl group were observed around 1238 cm^{-1} (the amide III band). The ADM incorporating CNTs and copper microspheres exhibited a similar infrared spectrum, possibly because the absorption peak of collagen covered its absorption peak. From the above characterization results, it can be seen that our simple experimental design could retain the natural structure of ADM to a large extent, and on this basis, substances were firmly combined in the scaffolds to improve the performance of e-ADM. For the Raman spectrum of CNTs (Figure 2F), the typical peaks appeared at 1350 and 1580 cm^{-1}. The peak of 1350 cm^{-1} was D, and its strength corresponded to the defects and disorders of CNTs. The peak at 1580 cm^{-1} was G, and its strength corresponded to the integrity of CNTs. The typical peaks of CuO microspheres appeared at 200, 295, and 628 cm^{-1}. These three Raman peaks were related to the vibration mode of the Cu–O bond. Raman spectroscopy and mapping further illustrated that the sample consisted predominantly of copper oxide from the perspective of valence bonds. However, the C element provided by CNTs was not evenly distributed on the surface of the scaffold. Because of its small size, it could easily enter the scaffold through gaps between micro and nanofibers, and the results of Raman mapping (Figure 2G) supported this view. A very small amount of CNTs were present on the surface of the scaffold. Due to the uneven structure and tiny pores on the ADM surface, the density of CuO on the ADM surface is relatively concentrated, but not uniform enough. The basic principle of atomic force microscopy (AFM) is to obtain the structural information of the material surface by measuring the weak interaction force between the probe and the object's surface (Figure 2H). The e-ADM exhibited a dense arrangement, and the natural banding period patterns (around ≈67 nm) of collagen fiber bundles in e-ADM further illustrated the scaffold material's retention ability for effective dermal tissue components. The ultra-depth-of-field microscope was used to obtain multiple photographs with different focal lengths in a fixed height range and analyzed the surface smoothness and other information of the object to be tested. The photograph (Figure 2I) showed that the surface of the e-ADM bracket was dark blue, and the height difference was 225 μm cm^{-2} per unit area. This flat surface structure facilitates the integration of the wound, better exerting antibacterial and promoting wound repair functions. An energy-dispersive X-ray spectrometer (EDS) was used to analyze the material's composition. The cross-sectional spectral line scanning images of e-ADM (Figure 2J) showed that Cu was evenly distributed inside the scaffold, and the line of best fit was distributed between 500 and 600 cnt. In the surface spectral surface scan results of e-ADM (Figure 2K), the collagen component contributed to three elements C, N, and O. In addition, Cu was evenly distributed on the surface of the scaffold.

2.2. Mechanical Properties, pH-Responsive Antibacterial Properties, and Biodegradability of e-ADM

85% of the collagen in animal skin is type I collagen, which has a complex multi-level spatial structure.[27] First, the α chain of (Gly-X-Y)n (n = 350, X is proline, Y is hydroxyproline) forms the most basic triple helix structure under the action of hydrogen bonds. The triple helix and adjacent microfibers exhibit a "D-banding" unit. The original fiber continues to grow and forms the 3D supra-fibrillar network structure, providing scaffolding structures of the body tissues and the bespoke natures of the tissues from the nanoscopic to macroscopic length scales. On this basis, the residual cells and other components of ADM retain the original biocompatibility of animal skin. It is worth mentioning that copper ions introduced in the system can also improve mechanical strength, and the specific mechanism is shown (**Figure 3**A). This mechanism is derived from the "tanning" effect in the leather production process. First, copper ions enter the leather fibers through osmosis and undergo hydroxyl and oxygen polymerization in the aqueous solution environment. Finally, chemical crosslinking occurs between two or more fibers. The carboxyl groups that provide the reaction sites can be derived from the protein molecule's terminal carboxyl or R-terminal anhydride. In addition to the tanning effect mentioned above, the added copper molecules and CNTs are smaller than those between fiber bundles, playing a filling role. The chemical crosslinking and physical filling account for improved mechanical properties of e-ADM (Figure 3B). First of all, due to the limited mechanical strength provided by collagen fibers, the tensile strength of ADM is only 13 MPa. The ADM after adding CNTs was destroyed at a lower tensile strength, which may be due to the limited filling effect of CNTs on ADM, and the toughness of ADM was reduced because the water was completely removed during freeze-drying. Importantly, we found that the addition of copper oxide microspheres significantly improved the tensile strength of the scaffolds. When the addition of copper microspheres was 2%, 5%, and 10%, the tensile strength reached 18, 23, and 25 MPa, respectively. However, considering the cytotoxicity caused by excessive copper incorporation, the amount of copper oxide added was finally set to 5%. We found that a series of skin scaffolds had good tensile resistance, but the ability to resist strain was poor. Considering that the final material was used as skin scaffolds, much emphasis was placed on the tensile properties. Similar fiber scaffolds in the literature are mentioned in this article. By comparing the mechanical properties (Figure 3C), we found that e-ADM exhibited the best performance. Skin scaffold is hydrophobic when exposed to water. The water contact angle test illustrates the ability of a skin scaffold to absorb fluid (Figure 3D). However, due to a

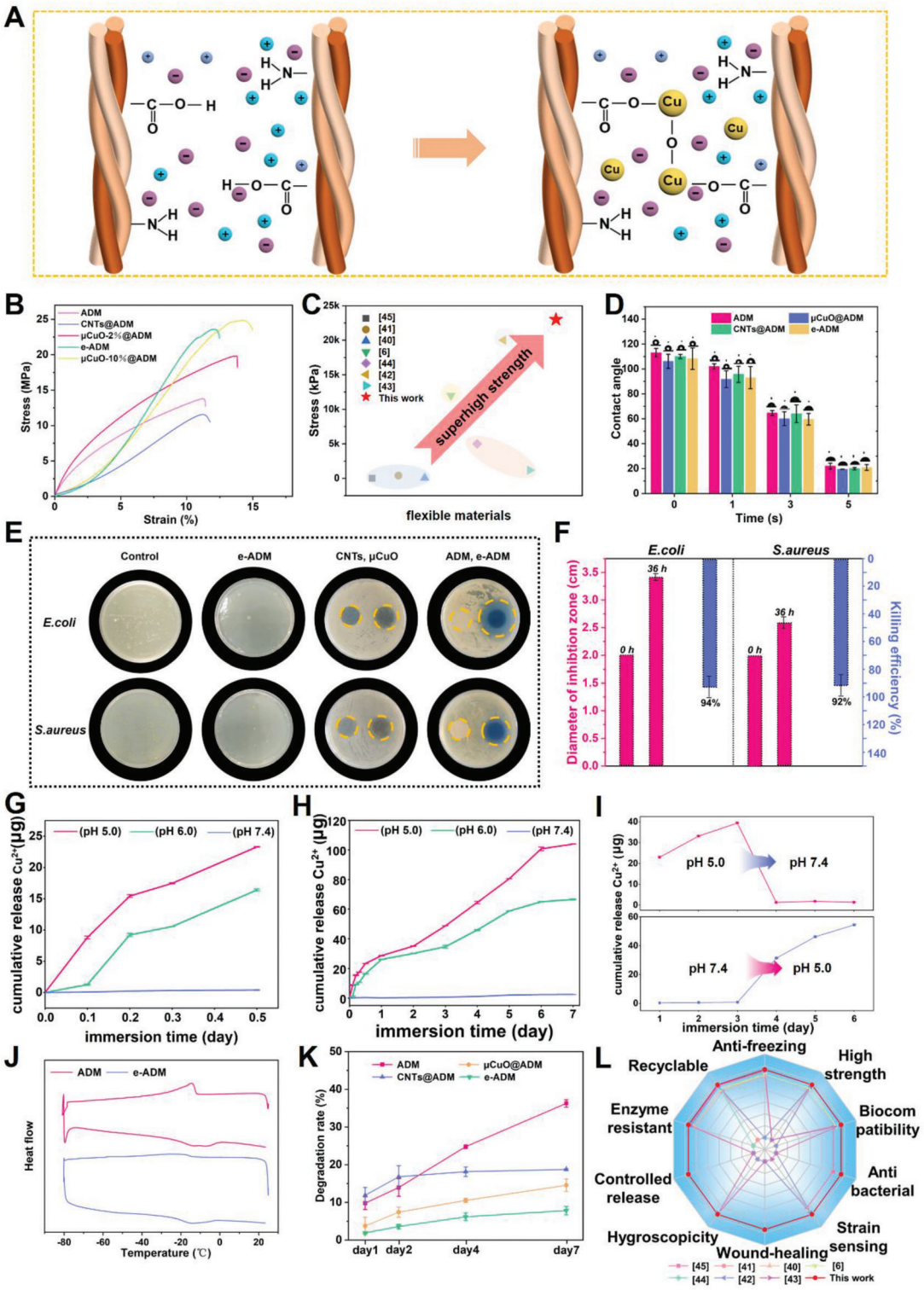

Figure 3. Multifunctional display of e-ADM. A) Mechanism diagram of ADM and ADM after crosslinking. B) Tensile test results of a series of skin scaffolds. C) Comparison of tensile properties between e-ADM and previously reported electronic skin scaffolds. D) Water contact angle test results of a series of skin scaffolds. E) Bacteriostasis rate of ADM and e-ADM, inhibition zone photo. F) Bacteriostasis rate and inhibition zone size. G) Released amount of copper ions in PBS buffer solution with different pH in 12 h. H) Released amount of copper ions in PBS buffer solution with different pH in 7 days. I) Controlled release of copper ions with pH changes. J) DSC test results of ADM and e-ADM. K) Enzyme degradation of a series of skin scaffolds. L) Comparison between e-ADM and previously reported scaffold material for skin tissue (yes stands for the presence of this function; no means absence or lack of corresponding data or proof about the function). Data are depicted as mean ± SD (n = 6), and analyzed by one-way ANOVA with Tukey's multiple comparison test compared to the ADM group.

large number of pores on the surface of scaffolds and collagen fibers' hydrophilic properties, water was almost instantaneously sucked into the scaffolds. After 5 s, the water contact angle of the skin scaffolds was only about 20°.

Copper has been used as an antibacterial agent for thousands of years. It has been established that copper has efficient, broad-spectrum, and durable antibacterial properties. At present, little is currently known about the antibacterial mechanism of copper. However, the antibacterial mechanism of copper oxide microspheres used in this article came from the following two simple processes. Due to the resistance to traditional antibiotics, much emphasis has been placed in recent years on the design of preventive antibacterial strategies on the surface of materials, such as the design of new materials by simulating nanopillars on cicada wings in nature. The cell membrane of bacteria was subjected to tensile and shear forces after coming in contact with the nanocolumn, resulting in cell rupture and death. The initial contact between the bacteria and the material's surface is mainly due to interactions such as hydrophobicity of the material surface and physical adsorption. This physical mechanism is mostly used by Gram-negative bacteria given their thinner bacterial membrane (Gram-negative bacteria 2–3 nm, Gram-positive bacteria about 20 nm). Of course, this physical antibacterial process is cheap and environmentally friendly and does not lead to drug resistance. The other antibacterial mechanism is known as the antibacterial process of metal ions, the specific antibacterial mechanism can be found in Figure 1B,E. Importantly, our e-ADM showed a good antibacterial effect under the combined action of the two antibacterial processes, and the antibacterial rate was calculated by the colony counting method(Figure S3, Supporting Information), and the diameter of the antibacterial circle was measured by the antibacterial circle method (Figure 3E,F). Some Gram-positive bacteria with hard-to-break cell walls, such as *Staphylococcus epidermidis* and *Enterococcus faecalis*, e-ADM also has a strong antibacterial ability, the inhibition zone test photo is placed in the Supporting Information (Figure S4, Supporting Information). The bacteriostatic rate of e-ADM against *Escherichia coli* reached 94%, and the bacteriostatic circle of nearly 3.5 cm substantiated a good antibacterial effect against *E. coli*. The bacteriostatic rate of *Staphylococcus aureus* and the diameter of the bacteriostatic circle were 92% and 2.5 cm, respectively. This finding confirms that Gram-positive bacteria have a thicker cell wall and membrane. It can be concluded that these two pathogenic bacteria can be effectively inhibited when clinically applied.

Recent studies found that copper and silver exhibit cytotoxicity in a high-concentration environment for sustained periods. Accordingly, it is necessary to establish a controlled-release antibacterial system. The physiological environment of the skin is often subject to two major changes: temperature rise and pH decrease, and the acidification of the physiological environment is the result of bacterial metabolism. It is widely acknowledged that the pH of the normal physiological environment of the human body is about 7.4, but the pH can reach 5 when the bacteria are growing. Accordingly, the principle of designing a precise copper ion controllable release system is explained from two aspects. The release of copper ions is partly due to the ionization of copper oxide microspheres embedded in ADM. A high concentration of H^+ drives Cu^{2+} into the solution system. In this process, the copper oxide microspheres provide more pores and a larger surface area, which is more conducive to releasing copper ions. Moreover, the release of copper ions comes from the "tanning" binding site mentioned above. It is well-established that an important process called "alkali extraction" occurs in the middle and later stages of the leather tanning process, accompanied by further crosslinking and fixation of chemical sites in leather during the alkali extraction process. This process is reversible based on pH changes in the solution system. For sites that have been combined, re-increasing acidity could lead to the re-separation of metal coordination ions into the environment, providing another release mode of copper ions, although only trace amounts were observed. Inductively coupled plasma (ICP) can be used to analyze the geo elements in the solution system. The cumulative release of copper ions in e-ADM immersed in phosphate-buffered saline (PBS) solution of different pH for a certain time, within 12 h (Figure 3G), within 7 days (Figure 3H), and pH change (Figure 3I) were measured by ICP. Within the first 7 days, there was almost no increase in Cu^{2+} in PBS solution with pH 7.4, and the content in the system was not more than 0.1 μg, which was within the safe range of human beings for copper. When the pH was 5 and 6, we found that the content of Cu^{2+} significantly increased, especially when the pH was 5, and the copper content reached more than 100 μg after 7 days. This long-term release of copper ions could ensure the reliability of sterilization. A validation experiment was designed to verify the controlled release system's performance. At the end of the third day, the pH of the PBS solution was adjusted from 5 to 7.4 and from 7.4 to 5, respectively, and the results were consistent with expectations. Within 1 day after the pH change, the concentration of copper ions decreased to human safety concentration and increased to the minimum inhibitory concentration (MIC), respectively. It was confirmed that good pH responsiveness ensured the slow release of copper ions to the trauma site in a physiological environment (pH 7.4). An increasing body of evidence suggests that low concentrations of copper ions can promote vascular endothelial growth factor (VEGF) production, thereby promoting vascular endothelialization, and inhibiting smooth muscle cell proliferation and thrombosis. Animal verification experiments will be mentioned later.

Differential scanning calorimetry (DSC, Figure 3J), and degradation resistance test (Figure 3K) were used for the verification of the good performance of the skin scaffold experiment. The DSC test results showed that the freezing point of ADM was approximately −20 °C, while the DSC curve of e-ADM was smoother, and there was no obvious freezing point near −20 °C, indicating that the skin scaffold exhibited frost resistance. Good resistance to degradation can ensure better performance of skin scaffolds and reduce the number of dressing changes. The test results showed that the internal crosslinking degree of ADM is not high and can be easily decomposed by protease. The degradation rate reached 37% after 7 days. After undergoing a series of crosslinking and filling, the skin scaffolds exhibited better degradation resistance, and the degradation rate of e-ADM was not higher than 10% after 7 days. Compared with the electronic skin or hydrogel mentioned above,[6,40–45] e-ADM performed better in many aspects (Figure 3L).

2.3. e-ADM for Real-Time Monitoring of Large-Scale Human Motion

Given that the internal network structure of ADM consisted of natural tissue, it could exhibit mechanical and physiological characteristics similar to human skin and organs. In this study, we recorded changes in electrical signals during various physical activities including chewing, swallowing, joint bending, wrist bending, knee bending, and plantar pressure (**Figure 4**Q). For such activities, e-ADM should have excellent pressure sensitivity and plasticity ($R/R0$ = (D-value of resistance)/initial resistance × 100%). It was observed that different deformations of e-ADM could produce changes in the relative resistance value since different deformation methods cause changes in the internal resistance value to varying degrees. For example, stretching and torsion could improve conduction since such deformation induced a close arrangement of the internal channels. It is worth mentioning that e-ADM could respond to most deformations including subtle activities such as swallowing and chewing. These subtle electrical signals were collected to complete human–computer interaction and physiological monitoring. In addition, e-ADM could sustain different degrees of deformation, bending, torsion, pressing, and stretching (Figure 4A–C,E). When different forces were applied, the resistance exhibited different changes in size, and the change was often instantaneous, indicating a rapid response. We further found that when the torsion angle was fixed or stretched until it was deformed (Figure 4D,F), more consistent changes in resistance were observed, which enabled the differentiation of different deformation sizes.

Similarly, different parts of the body can produce different types of deformation. Collecting these signals through e-ADM as a sensor enables body monitoring and human–computer interaction (Figure 4G–P). In this paper, the signals for the most common deformations were recorded. The results showed that the recorded signals were relatively stable, and relatively small deformations were accompanied by a certain degree of resistance change. In addition, when e-ADM was attached to the elbow and knee, the rapid and repeated deformation did not affect the sensing performance. A more intuitive video demonstration (Videos S1 and S2, Supporting Information) to more intuitively reflect the performance of e-ADM in monitoring human motion. In summary, when e-ADM is used as a sensor, it has a fast response, visible deformation, and stability, suggesting it has huge prospects for application in different scenarios.

2.4. Biocompatibility of e-ADM

The use of powerful antibacterial materials, including silver nanoparticles, quaternary ammonium salts, and other materials, has been limited in the medical field. The severity of cell toxicity is affected by the size, shape, surface modification, charge aggregation, and type of material. Studies have shown that electrical stimulation can accelerate cell growth and proliferation in several ways (**Figure 5**A), such as changing the potential difference on both sides of the cell membrane to guide more calcium ions to flow into the cytoplasm and activate growth factor expression. Moreover, electrical stimulation can reportedly accelerate adenosine triphosphate (ATP) consumption while promoting cell metabolism, thereby altering membrane-related behaviors such as endocytosis, adhesion, and migration. Electrical stimulation can also control the generation of reactive oxygen species (ROS) and promote the proliferation and differentiation of mesenchymal stem cells. To verify the biocompatibility of e-ADM under conventional state and micro-current stimulation, methylthiazolyl tetrazolium (MTT) co-culture and laser scanning confocal microscopy (LCSM) were used to photograph live dead cells after fluorescence staining. A self-made device (Figure 5B) was used in the experimental group of electrical stimulation. A hole with a diameter of 0.5 cm was set at the bottom of the six-hole plate to form an electrical circuit, and the agar salt bridge was used to prevent direct contact between the electrode and the medium. Chinese hamster lung (CHL) cells were used to evaluate the scaffold's biocompatibility. The results showed that with the introduction of copper microspheres and electrical stimulation, the corresponding cell viability was slightly lower than the control group, suggesting no significant cytotoxicity (Figure 5D), which is acceptable for the application of biomaterials. In addition, the LCSM images of CHL cells on the scaffold showed good cell growth and distribution, and no obvious cell death was observed (the survived cells were green, and the dead cells were red), suggesting good biocompatibility (Figure 5C). The flow cytometry results of a series of skin scaffolds showed that all the counts fell in the Q4 region, that is, the cells were all alive, which verified the excellent biosafety of e-ADM (Figure 5E). In addition, the chemical crosslinking formed within the scaffold was very stable in a physiological environment (pH 7.4), consistent with the ICP test results. Overall, the e-ADM scaffold has good physical and chemical properties and antibacterial effects and supports cell adhesion, growth, and proliferation.

2.5. e-ADM Under Electrical Stimulation for Full-Thickness Skin Wound Healing

It is well-established that the recovery process of skin tissue defects includes granulation tissue and scar formation. The basic wound healing process encompasses acute inflammation, cell proliferation, scar formation, epidermis, and other tissue regeneration. Two symmetrical full-thickness skin defect wounds were opened on the back of specific pathogen-free (SPF) rats (**Figure 6**A). The skin scaffold was placed in one defect (TEG), and no material was placed in the other (TCG). Intermittent microcurrents were used to verify the effect of electrical stimulation on skin reconstruction. Photos of wounds on days 0, 3, 7, and 15 of different treatments (Control, ADM, ADM-ES, e-ADM, and e-ADM-ES) were taken. A 2D model of the rat wound was established to better compare the healing situation (Figure 6B). In the early stage, the bacteria around the wound proliferated actively, and the bacterial metabolism caused the physiological environment to be acidic. A large amount of copper ions were excluded from the environment filled with body fluids to contact with the skin so that the positive expression of wound healing in the e-ADM experimental group was poor within ≈0–3 days. As the bacteria were killed, the physiological environment developed into neutral, and the lethality of copper ions quietly withdrew. Low-dose copper ion expression promoted vascularization and cell proliferation, and cells adhered and grew on ADM. On

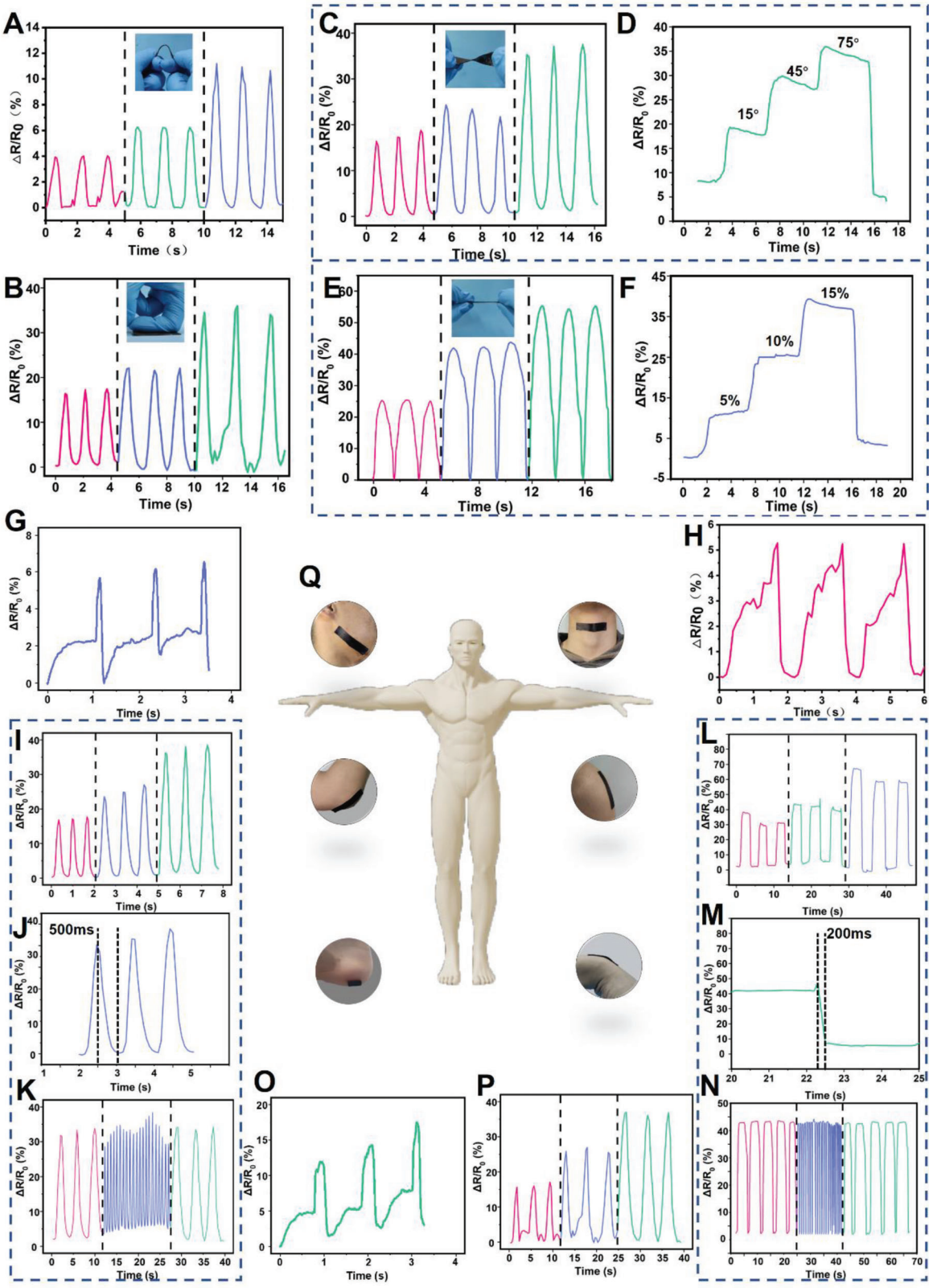

Figure 4. Monitoring of joint movement and electrochemical properties of e-ADM. A) Bending, B) pressing, C) twisting, D) twisting to a fixed angle, E) stretching, and F) stretching to a fixed deformation. Put e-ADM on G) chew, H) vocal cord, I) elbow, J) response time, K) elbow activity at different frequencies, L) knee, M) response time, N) knee activity at different frequencies, O) plantar, and P) wrist relative resistance change rate. Q) Schemata of human models. Photo and video credit: Institute of Biomass & Functional Materials, Shaanxi University of Science & Technology.

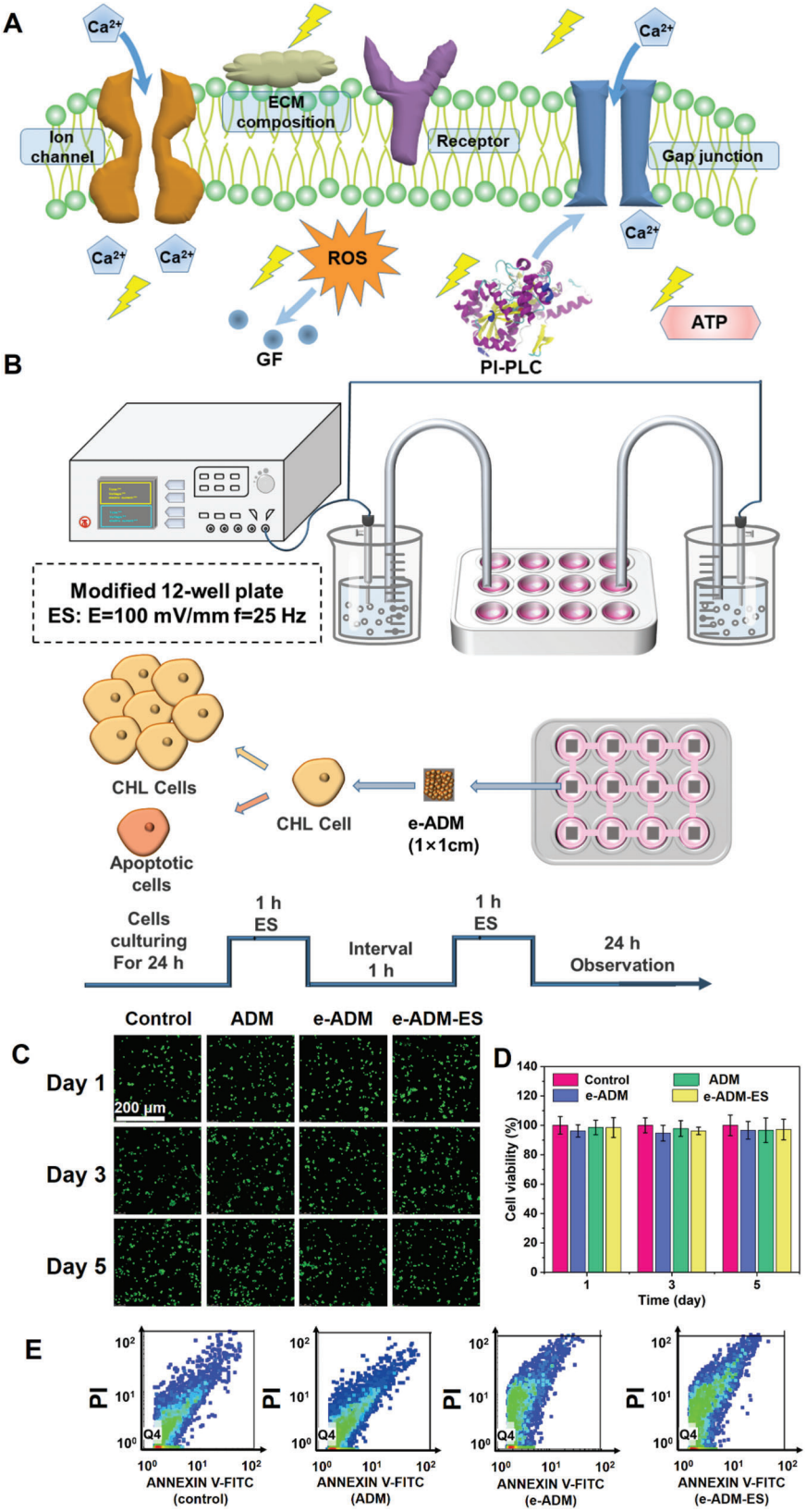

Figure 5. Biocompatibility of e-ADM. A) Regulatory mechanism of microcurrent stimulation in cells. B) Device used to verify the effect of microcurrent on cells. C) LSCM images of Live Dead staining and D) cell viability after a period of time. E) Flow cytometry results of a series of skin scaffolds. Data are depicted as mean ± SD ($n = 6$), and analyzed by one-way ANOVA with Tukey's multiple comparison test compared to the control group.

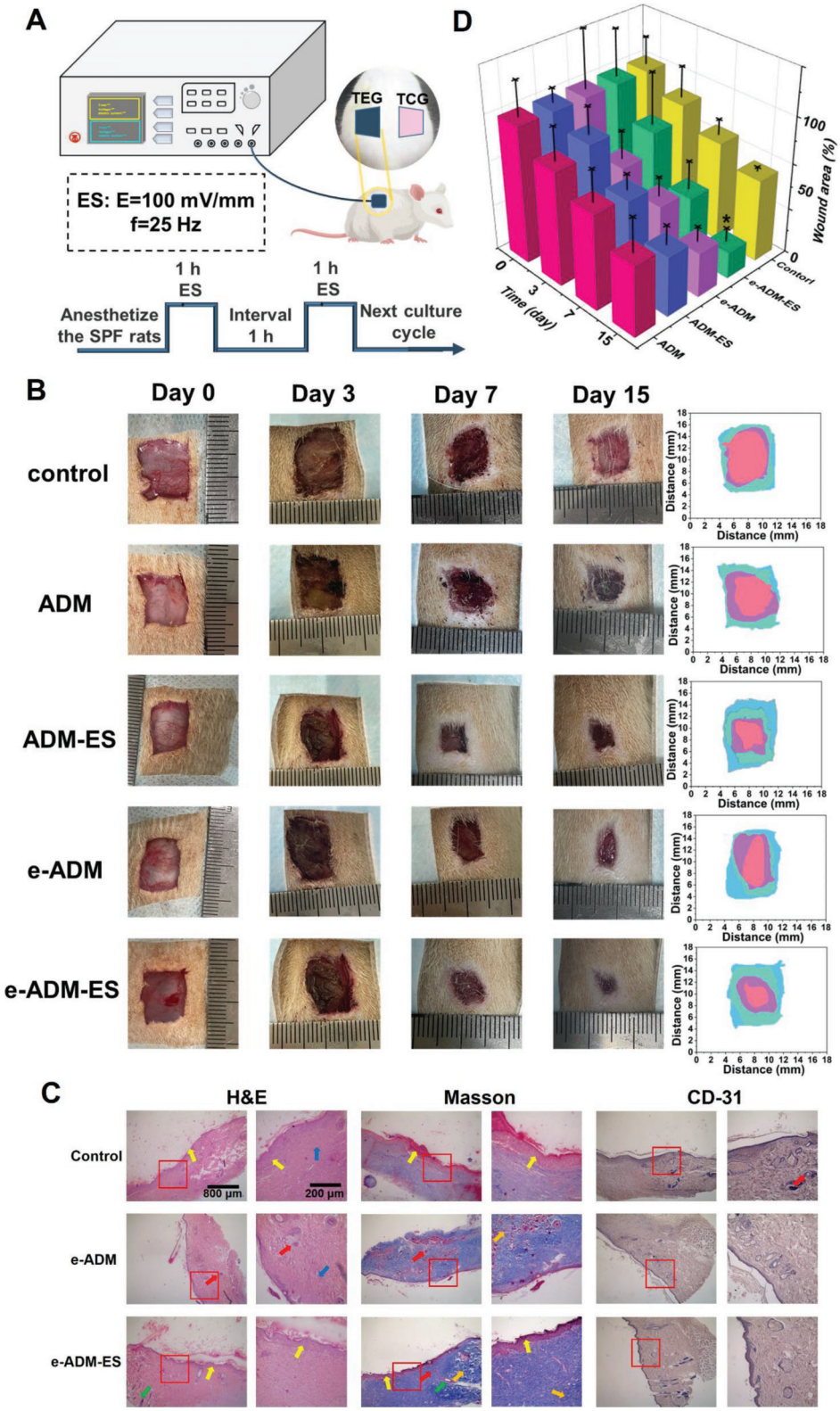

Figure 6. Repair of full-thickness skin defects in SPF rats. A) Devices and parameters for electrical stimulation therapy. B) Comparison of full-thickness skin defect repair photos and wound models of SPF rats in coordinates (blue-Day0, green-Day3, purple-Day7, pink-Day15). C) H&E staining, Masson staining, and CD-31chemical staining of wound tissue on day 15 blood vessel (red arrow), fibroblast (yellow arrow), neutrophil (blue arrow), hair follicle (green arrow), and collagen deposition (orange arrow). D) The wound area (%) decreased within 15 days under the five treatments. Data are depicted as mean ± SD ($n = 6$), and analyzed by one-way ANOVA with Tukey's multiple comparison test compared to the control group.

the 7th day, it can be observed that the introduced copper element and biological microcurrent play a significant role in promoting vascularization expression and cell proliferation, and the positive expression of wound healing is more perfect. On the 15th day of treatment, the healing degree of the control group was the lowest, and the wound area was 60% of the original. Compared with the control group, the skin wound area of the ADM treatment group was significantly reduced (52% vs 60%) (Figure 6D). It has been confirmed that ADM has brought significant benefits for skin wound treatment and skin reconstruction. The activation of growth factors and the activity of cells and blood vessels between fibers with gaps help to significantly improve the healing rate. The positive expression of wound healing in the ADM-ES experimental group was strong (wound area 44%), which can prove the significant promoting effect of simulated human microcurrent on wound healing. The wound area of the e-ADM treatment group was 32.7%, and the introduction of copper is the main reason for the excellent therapeutic effect of e-ADM. Low-dose copper activates hypoxia-inducible factor-1 (HIF-1) and promotes new angiogenesis. In the e-ADM-ES treatment group (wound area 19.3%), copper and biological micro-currents work together on the cells at the wound and accelerate vascularization, and the wound can complete 80% of the new skin reconstruction in a faster time.

To further evaluate the performance of the e-ADM scaffold in skin reconstruction, the tissue sections of rat wounds were observed and analyzed by immunohistochemical staining (hematoxylin-eosin staining [H&E], Masson, Platelet endothelial cell adhesion molecule-1[CD31]). The microphotographs of wound tissue sections under different treatment methods on day 7 are shown (Figure 6C), and more information can be found in the Supporting Information (Figures S4–S6, Supporting Information). H&E staining was used to observe wound healing. Masson staining can reflect the growth of collagen fibers in the wound. CD31 can specifically stain platelet-endothelial cell adhesion molecules and play an important role in interacting with neutrophils. To facilitate observation and analysis, the important factors in the photograph results were marked including blood vessels in the wound area (red arrow), fibroblasts (yellow arrow), neutrophils (blue arrow), hair follicles (green arrow), and collagen deposition (orange arrow). Compared with the control group, a larger number of wound fibroblasts were found in the e-ADM and electrical stimulation treatment groups with a thicker epidermis. The H&E staining results showed the least number of neutrophils in the electrical stimulation treatment group, which proved less inflammation in the wound. Masson staining showed that the treatment group had more collagen fiber deposition, especially the collagen fiber accumulation in the electrical stimulation treatment group was the densest, the deposition of collagen fibers was almost consistent with that of intact skin. In addition, the expression of CD31 in the e-ADM and electrical stimulation treatment groups were higher, and the process of fibroblasts, keratinocytes, granulation, and reepithelialization in the observed area was better, consistent with the results of H&E staining and Masson staining. Under the stimulation of bionic micro currents, low concentration of copper ions, and ADM substrate, optimal wound repair was achieved.

In summary, a hitherto undocumented ADM-based bioelectronic skin (e-ADM) was fabricated for implementation as "wound therapy monitoring" tissue-nanoengineered skin scaffolds. A facile "one-pot" bio-compositing strategy of nature ADM was used to incorporate the functional building blocks of conductive CNTs and self-assembled micro-copper oxide microspheres with a cicada-wing-like rough surface and nanocone microstructure. With a multifunctional and bionic-structure design, e-ADM exhibited robust tensile strength, antibacterial properties, flexibility, biodegradability, electroactivity, biocompatibility, and the pH-responsive ability for intelligent command between sterilization (pH ≈5–6) and wound repairing (pH 7.4) as expected. Moreover, the real-time large-scale human motion monitoring ability of the e-ADM provided the platform to design implantable "health monitoring" tissue-nanoengineered skin scaffolds. Additionally, e-ADM under precise electrical stimulation could facilitate cell growth and proliferation and therefore promote the in vivo full-thickness skin wound healing with apparent trauma area reduction, granulation tissue palingenesis, collagen deposition enhancement, vascularization, and reepithelialization, leading to a novel, versatile, and high-performance "wound therapy monitoring" implantable bioelectronic skin (bio-e-skin) for real-world biomedical applications.

3. Experimental Section

Fabrication of Copper Oxide Microspheres: The process of μCuO production is listed in Figure S1, Supporting Information. The porous copper oxide microspheres (μCuO) were prepared by a hydrothermal method. Specifically, 4.832 g of copper nitrate hydrate $Cu(NO_3)_2 \bullet 3H_2O$ was mixed with 30 mL of ethanol, 20 mL ammonia-water (25%), and 20 mL of sodium hydroxide (1 M). This mixture was transferred into a hydrothermal reactor and heated at 120 °C for 4 h. After that, μCuO was collected by centrifugation, washed three times with deionized (DI) water, and dried in an oven at 60 °C for 12 h.

Fabrication of ADM: ADM used in this study was derived from the processing of pig skin. In short, fresh pig skin was obtained from a local slaughterhouse (Xi'an, China). Pig skin slices with a thickness of 10 × 10 cm were taken from the back of fresh pig skin. At 30 °C, the pig skin slice was thoroughly washed in water (500% of skin weight) containing flat addition (0.5% of skin weight) and the subcutaneous fat was removed manually. Then, at 30 °C, the pig skin slice was rotated in a drum containing sodium carbonate (2.5% of skin weight) and flat addition (1% of skin weight) for 6 h. At 25 °C, the meat side of the pig skin slice was coated with trypsin (2.5%, 250 U mg^{-1}) overnight to remove the hair. Alkaline enzymes were added to remove impurities and purify the pig skin tissue. The ADM scaffold was finally obtained after freeze-drying the porcine skin slices that were thoroughly washed.

Fabrication of e-ADM: ADM with a weight of 1 g was placed in a mixed solution of 1.5 mL MWCNTs-COOH and 8.5 mL DI water for ultrasonic treatment for 2 h, and 0.5 mL μCuO (1 M) was added to the mixed solution and shaken at 37 °C for 12 h (250 rpm). Then, the sample was washed using ultrapure water and lyophilized before testing.

Surface Characterization: The surface morphology and elemental component of the e-skin were characterized by a field emission scanning electron microscope (FE-SEM, S-4800, Hitachi, Japan) equipped with EDS. The surface morphology of ADM scaffolds was further observed by atomic force microscope (AFM, SPM-9600, SHIMADZU, Japan) and 3D digital microscopy (HIROX, Japan). ADM scaffolds were dried by freezer dryer and tested by FT-IR spectroscopy (Perkin Elmer FT-IR Spectrum Two, USA). Raman spectra (RS) were measured in a laser-scanning confocal micro-Raman spectrometer. The ADM scaffolds were placed on a microslide and detected by the laser micro-Raman imaging spectrometer (THEM DXRxi, USA).

Thermal Stability Analysis: The ADM scaffolds were characterized by a differential scanning calorimeter (DSC Q2000 V24.11 Build 124, TA Instruments, USA) to analyze the movement of polymer chains from inside of ADM under a nitrogen atmosphere. ADM scaffolds of 3.4 mg were put into aluminum pans, hermetically sealed, and scanned over the temperature range of 20 to −80 °C at a heating rate of 5 °C min^{-1}. The empty aluminum pan was used as a reference. Prior to measurement, the ADM scaffolds were freeze-dried under a vacuum.

Cu^{2+} Release into Phosphate Buffer Solution: To investigate the release behavior of Cu^{2+} into PBS, an ICP-atomic emission spectrometer (THEM, USA) was utilized to measure the concentration of ions in the solution. Briefly, specimens were immersed into 10 mL of PBS with different pH (pH = 7.4, 5) at 37 °C for 7 days. At predetermined time points, the entire volume of solution was collected and samples were refilled with fresh PBS. The concentration of Cu^{2+} in the collected solution was determined by ICP. To further explore the pH-responsive release of metal ions, samples were immersed in 2 mL of PBS with a pH of 7.4 in the first 3 days and then immersed in PBS with a pH of 5 for another 3 days. The solution was collected and refilled at predetermined time points and the concentration of metal ions was determined by ICP.

Mechanical Properties: The tensile strength of ADM scaffolds with an original gauge length of 10 mm was tested at a tensile rate of 10 mm s^{-1} using an electromechanical tensile testing machine (AI-7000-NGD, Gotwell Dongguan Co., Ltd).

Antibacterial Properties: The antibacterial test of ADM scaffolds was characterized by measuring the inhibition zone and counting the colonies. The ADM scaffolds were cut into discs (1 cm in diameter) and then placed on Müller–Hinton agar and plates containing *E. coli* and *S. aureus*. The plates were then stored at 37 °C for 24 h. After this period, the radius of the inhibition zone was accurately measured by a caliper. Original bacterial suspensions were washed three times with PBS (pH 7.4) solution to a concentration of 108 CFU mL^{-1}. Then, the samples were poured into the washed culture medium and incubated in a shaking bath for 1 h. The incubated solution was diluted five times to a certain concentration. The resulting bacterial PBS suspensions were spread on gelatinous LB agar plates, and cultured at 37 °C for 24 h. The number of survival colonies was counted manually. The tests were repeated three times for each bacteria. In particular, glassware, suction nozzles, and culture medium were sterilized in an autoclave at a high pressure of 0.1 MPa and a temperature of 120 °C for 30 min before experiments.

Conductive Tests: The conductivities were characterized by using a Multifunctional Digital Four-probe Tester. (ST-2258C, Beijing Tongde Venture Co., Ltd.). The ADM scaffolds used as compression sensors were cut into squares (50 mm × 20 mm × 0.5 mm). Nickel foam tapes were attached to both ends of the conductive ADM scaffolds to form a strain sensor. Subsequently, the sensor was attached to different positions of an observer (first joint of the forefinger, elbow, opisthenar, and wrist) to detect electrical signals. According to the institutional review and approval of the Ethics Committee of Shaanxi University of Science and Technology (2 021 008), human subjects were studied. Volunteers were informed and agreed to the measured risks and benefits.

In Vitro Enzymatic Degradation: To characterize the degradation properties of the material, dry ADM and e-ADM scaffolds were cut into quarter-sized pieces, weighed (denoted as W1), then soaked in collagenase type I/PBS solution (1 U mL^{-1}, 3 mL mg^{-1} sample) for 7 days at 37 °C. The collagenase/PBS solution was changed every 2 days. To measure the degradation rate, samples were removed from the collagenase/PBS solution on days 1, 2, 4, and 7, then rinsed with PBS followed by distilled water. The samples were lyophilized and weighed (denoted W2). The degradation rate was calculated using the formula

$$\text{Degradation rate } (\%) = \frac{W_1 - W_2}{W_1} \times 100 \quad (1)$$

Biocompatibility Evaluation: The cytotoxicity of the ADM scaffolds was evaluated with MTT assays; Live/Dead samples (epithelial cells of hamster lung) were visualized using a Calcein-AM/PI Double Stain Kit and a Leica TCS SP8 STED inverted confocal microscope.

Assessment of the Ability to Promote Cell Proliferation: The skin scaffolds were co-cultured with CHL cells under electrical stimulation with special equipment. The following ES scheme was adopted: After 1 day of cultivation, the e-ADM group underwent electrical stimulation for 7 days. The electric field intensity was 100 mV mm^{-1} (frequency = 25 Hz) at intervals of 24 h. During one period, ES was performed twice for 1 h, with an interval of 1 h between each time. The cell proliferation rate was monitored by an inverted confocal microscope (DMi8) and flow cytometry (FACSCalibur).

In Vivo Full-Thickness Skin Defect Model: SPF rats (6–8-week-old and 180–220 g) were obtained from the Institute for Hygiene of Ordnance Industry (Xi'an, China). They were maintained with free access to pellet food (Jiangsu Xietong Biotechnology Co., Ltd, Nanjing, China) and water in plastic cages at 18–26 °C and kept on a 12-h light/dark cycle. Animal welfare and experimental procedures were carried out strictly in accordance with the guide for the care and use of laboratory animals (Shaanxi Province Science and Technology Department of China, 2016) and the related ethical regulations of the Institute for Hygiene of Ordnance Industry. All efforts were made to minimize animal suffering and reduce the number of animals used. A square full-thickness wound with a length of 1 cm was created by a punch on the back of SPF rats. The rats were divided into four groups: e-ADM-ES group, e-ADM group, ADM group, and control group. The same ES scheme as above was adopted. The wound areas were first photographed, and the tissue specimens were stained with H&E staining, Masson staining, and CD31 staining until the wound almost healed.

Statistical Analysis: Data are depicted as mean ± SD ($n = 6$), and analyzed by one-way ANOVA with Tukey's multiple comparison test compared to TCG. The level of significance was set at $*p < 0.05$, $**p < 0.01$, $***p < 0.001$.

Supporting Information

Supporting Information is available from the Wiley Online Library or from the author.

Acknowledgements

The authors sincerely acknowledge the funding and generous support of the National Natural Science Foundation of China (22278257), the Key R&D Program of Shaanxi Province (2022GY-272), the Chinese Postdoctoral Science Foundation (2021M692000), the Scientific Research Program Funded by Shaanxi Provincial Education (22JY013), and the Open Foundation of Key Laboratory of Auxiliary Chemistry and Technology for Chemical Industry, Ministry of Education, Shaanxi University of Science and Technology and Shaanxi Collaborative Innovation Center of Industrial Auxiliary Chemistry and Technology, Shaanxi University of Science and Technology (KFKT2022-11). The informed written consent from all human participants was obtained prior to the experiments, which were approved by Ethics Committee of Shaanxi University of Science and Technology (project number: 2022GY-272).

Conflict of Interest

The authors declare no conflict of interest.

Data Availability Statement

The data that support the findings of this study are available from the corresponding author upon reasonable request.

Keywords

antibacterial properties, bioelectronic skin-scaffolds, multi-functions, natural skin, wound therapy-health monitoring

Received: November 16, 2022
Revised: March 19, 2023
Published online: April 10, 2023

[1] H. Lim, H. S. Kim, R. Qazi, Y. Kwon, W. Yeo, *Adv. Mater.* **2020**, *32*, 1901924.
[2] Y. Zhang, T. H. Tao, *Adv. Mater.* **2019**, *31*, 1905767.
[3] Anonymous, *Nat. Nanotechnol.* **2017**, *12*, 1017.
[4] A. K. Dabrowska, F. Spano, S. Derler, C. Adlhart, N. D. Spencer, R. M. Rossi, *Skin Res. Technol.* **2018**, *24*, 165.
[5] M. Colonna, *Nat. Immunol.* **2010**, *11*, 1079.
[6] W. Zhang, B. Wu, S. Sun, P. Wu, *Nat. Commun.* **2021**, *12*, 4082.
[7] L. Chen, J. Ma, Y. Chen, C. Huang, Z. Zheng, Y. Gao, Z. Jiang, X. Wei, Y. Peng, S. Yu, L. Yang, *Biomater. Adv.* **2022**, *136*, 212790.
[8] S. Hou, Y. Liu, F. Feng, J. Zhou, X. Feng, Y. Fan, *Adv. Healthcare Mater.* **2020**, *9*, 1901041.
[9] A. N. Dalrymple, U. A. Robles, M. Huynh, B. A. Nayagam, R. A. Green, L. A. Poole-Warren, J. B. Fallon, R. K. Shepherd, *J. Neural Eng.* **2020**, *17*, 026018.
[10] J. Goding, P. Martens, L. Poole-Warren, R. Green, *Adv. Healthcare Mater.* **2017**, *6*, 1601177.
[11] M. Zheng, X. Wang, O. Yue, M. Hou, J. Guo, *Biomaterials* **2021**, *276*, 121026.
[12] X. Luo, Y. Liu, R. Qin, F. Ao, X. Wang, H. Zhang, M. Yang, X. Liu, *Appl. Mater. Today* **2022**, *29*, 101576.
[13] C. Ning, Z. Zhou, G. Tan, Y. Zhu, C. Mao, *Prog. Polym. Sci.* **2018**, *81*, 144.
[14] Z. Liu, X. Wan, Z. L. Wang, L. Li, *Adv. Mater.* **2021**, *33*, 2007429.
[15] A. J. Petty, R. L. Keate, B. Jiang, G. A. Ameer, J. Rivnay, *Chem. Mater.* **2020**, *32*, 4095.
[16] Y. Zhao, Z. Li, S. Song, K. Yang, H. Liu, Z. Yang, J. Wang, B. Yang, Q. Lin, *Adv. Funct. Mater.* **2019**, *29*, 1901474.1.
[17] M. Talikowska, X. Fu, G. Lisak, *Biosens. Bioelectron.* **2019**, *135*, 50.
[18] Y. Jiang, L. Liu, L. Chen, Y. Zhang, Y. Qin, *IEEE Sens. J.* **2021**, *21*, 12255.
[19] W. Luo, S. Q. Mei, T. Liu, L. Y. Yang, L. L. Fan, *Nanotechnology* **2022**, *33*, 135708.
[20] X. Bian, J. Xu, J. Yang, K. L. Chiu, S. Jiang, *Surf. Interfaces* **2021**, *23*, 100995.
[21] A. Rivadeneyra, A. Marín-Sánchez, B. Wicklein, J. Salmerón, A. Salinas-Castillo, *Compos. Sci. Technol.* **2021**, *208*, 108738.
[22] Y. Wang, F. Lu, E. Hu, K. Yu, R. Xie, *ACS Appl. Mater. Interfaces* **2021**, *13*, 16048.
[23] Y. Chen, N. Dan, W. Dan, X. Liu, L. Cong, *Mater. Sci. Eng., C* **2019**, *94*, 1020.
[24] L. Sun, L. Li, Y. Wang, M. Li, C. Zhang, *J. Tissue Viability* **2021**, *31*, 180.
[25] P. Loren, V. Michelle, M. Anna, *Oxid. Med. Cell Longevity* **2021**, *2012*, 1.
[26] H. Capella-Monsonís, M. A. Tilbury, J. G. Wall, D. I. Zeugolis, *Mater. Today Bio* **2020**, *136*, 212790.
[27] Y. Han, J. Hu, G. Sun, *J. Leather Sci. Eng.* **2021**, *3*, 4.
[28] Y. Liu, N. Nie, H. Tang, C. Zhang, J. Liu, *ACS Appl. Mater. Interfaces* **2021**, *13*, 11631.
[29] R. Liu, Y. Tang, H. Liu, L. Zeng, Z. Ma, J. Li, Y. Zhao, L. Ren, K. Yang, *Mater. Sci. Technol.* **2020**, *47*, 202.
[30] N. K. Yilmaz, C. A. Schiffer, *Chem. Rev.* **2021**, *121*, 3235.
[31] J. Yan, D. Xia, W. Zhou, Y. Li, P. Xiong, Q. Li, P. Wang, M. Li, Y. Zheng, Y. Cheng, *Acta Biomater.* **2020**, *115*, 220.
[32] S. M. Kelleher, O. Habimana, J. Lawler, B. O'Reilly, S. Daniels, E. Casey, A. Cowley, *ACS Appl. Mater. Interfaces* **2016**, *8*, 14966.
[33] H. Shahali, J. Hasan, A. Mathews, H. Wang, C. Yan, T. Tesfamichael, P. Yarlagadda, *J. Mater. Chem. B* **2019**, *7*, 1300.
[34] N. Verma, N. Kumar, *ACS Biomater. Sci. Eng.* **2019**, *5*, 1170.
[35] F. Sahin, N. Celik, A. Ceylan, M. Ruzi, M. S. Onses, *ACS Omega* **2022**, *7*, 26504.
[36] P. Liu, Z. Zhao, J. Tang, A. Wang, D. Zhao, Y. Yang, *ACS Biomater. Sci. Eng.* **2022**, *8*, 4976.
[37] X. Wang, Z. Liu, T. Zhang, *Small* **2017**, *13*, 1602790.
[38] X. M. Fu, *Adv. Mater.* **2012**, *562*, 490.
[39] X. Cheng, A. Fu, H. Li, Y. Wang, P. Guo, J. Liu, J. Zhang, X. S. Zhao, *ACS Sustainable Chem. Eng.* **2015**, *3*, 2414.
[40] X. Sui, H. Guo, C. Cai, Q. Li, C. Wen, X. Zhang, X. Wang, J. Yang, L. Zhang, *Chem. Eng. J.* **2021**, *419*, 129478.
[41] H. Liu, W. Zhao, G. Gao, X. Ren, *Mater. Today Commun.* **2019**, *21*, 100309.
[42] Y. Zhang, K. Chen, Y. Li, J. Lan, B. Yan, L. Shi, R. Ran, *ACS Appl. Mater. Interfaces* **2019**, *11*, 47350.
[43] B. Cheng, P. Wu, *ACS Nano* **2021**, *15*, 8676.
[44] H. Gong, Z. Xu, Y. Yang, Q. Xu, X. Li, X. Cheng, Y. Huang, F. Zhang, J. Zhao, S. Li, X. Liu, Q. Huang, W. Guo, *Biosens. Bioelectron.* **2020**, *169*, 112567.
[45] X. Peng, K. Dong, C. Ye, Y. Jiang, S. Zhai, R. Cheng, D. Liu, X. Gao, J. Wang, Z. L. Wang, *Sci. Adv.* **2020**, *6*, eaba9624.